

Probing Supermassive Black Hole Binaries with Orbital Resonances of Laser-Ranged Satellites

Minghui Du,¹ Qiong Deng,^{2,1} Yifan Bian,² Ziren Luo,^{1,3} and Peng Xu^{1,2,3,*}

¹*Institute of Mechanics, Chinese Academy of Sciences, Beijing 100190, China.*

²*Lanzhou Center of Theoretical Physics, Lanzhou University, Lanzhou 730000, China.*

³*Hangzhou Institute for Advanced Study, University of Chinese Academy of Sciences, Hangzhou 310124, China.*

The μHz gravitational waves (GWs) from coalescing supermassive black hole binaries (SMBHBs) carry extensive information which is valuable for the research of cosmology, astronomy, and fundamental physics. Before the operations of space-borne antennas like LISA and Taiji, current detectors are insensitive to GWs in this frequency range, leaving a gap to be filled with other methods. While, such GWs can induce lasting imprints on satellite orbit motions through resonant effect, and observational evidence for this phenomenon may be obtained via the satellite laser ranging (SLR) measurements. Our study is mainly dedicated to exploring the potential of SLR as a probe of GWs from SMBHBs. Based on previous work, we calculated the resonant evolutions of satellite orbits both numerically and analytically, and investigated the dependence on relevant parameters. Results of the signal-to-noise ratio (SNR) analysis showed that the imprint of an individual signal may not be quite remarkable, whereas before the operation of space-borne antennas, the possibility of discovering the first GW from a coalescing SMBHB with SLR missions is still promising. The thorough re-analysis of the documented data of SLR missions are also suggested.

I. INTRODUCTION

Ever since the landmark event GW150914 by the Adv-LIGO [1, 2], GW detections had opened the new window to our Universe, and with the observations in the following years of tens of signals ($1 - 10^3$ Hz) [3, 4] the new era for GW astronomy had gradually started off. In the next decade, space-borne antennas such as the Laser Interferometer Space Antenna (LISA) [5], the Taiji [6–9] and the TianQin missions [10] would cover the mHz band of the GW spectrum, and pulsar timing arrays is reported to be a promising probe for nHz GWs [11–13]. While, these approaches have left the μHz ($10^{-7} - 10^{-4}$ Hz) band unexplored in the foreseeable future.

In the late 1970s, Mashhoon and collaborators had studied the resonant responses of binary systems to incident GWs [14, 15]. Just like the case for a bound system of charged particles, which could have resonant interactions with incident photons when the photon frequency matches with the energy difference between certain states of the system. Likewise, the response of a self-gravitating binary system to GW is especially evident when the frequency of GW matches a harmonic of the binary’s orbital frequency, thereby inducing a resonance effect. Moreover, the secular evolution of the orbit may accumulate in time, and eventually enter the scope of detection.

The orbital frequencies of a large number of astronomical and man-made binary systems lie in the μHz band, which indicates that there is possibility to detect μHz GWs through their resonant effects on these systems. This idea has a long history but is not yet fully investigated [14–25]. Recently, Refs. [26, 27] placed constraints on the sensitivities of SLR, Lunar laser ranging

and pulsar timing arrays to the resonance due to stochastic gravitational wave background (SGWB), revealing the potential of bridging the μHz gap in the GW landscape.

Most of the GW signals studied in the aforementioned literature are stochastic in nature. As a complement, we are mainly interested in deterministic and individual signals with frequencies 10^{-5} - 10^{-4} Hz, such as the inspiral and merger phases of SMBHBs, which are among the strongest signals in this range. The identification of individual events gives more detailed properties of the sources. Especially, GWs from SMBHBs will provide extensive information about the coevolution of SMBHBs and their host galaxies, the growth of supermassive black holes, the strong-field, highly dynamic behavior of gravity, and the expansion history of the Universe [28]. LISA is also expected to detect SMBHBs, while 10^{-5} - 10^{-4} Hz corresponds to the less sensitive section of LISA’s frequency range. Moreover, due to the plentiful scientific objectives that can be achieved with SMBHBs, it would be of great significance if any detection of them can be made before the operation of LISA.

Except for SMBHBs, GWs generated by the population of DWDs in the Milky Way form a stochastic foreground at frequencies below mHz [29–32]. The orbits of DWDs are slow-varying, suggesting that their resonant effect can last for a long duration. Therefore, we will also briefly analyze the observable evidence of this foreground.

For clarity, if the GW source and the system affected by GW are both binaries, we will refer to the former as the “source binary” and the latter “test binary”. In this paper, we will adopt the system composed of laser-ranged satellite [33] and Earth as the test binary. On the one hand, the Earth-satellite distance can be measured precisely and continuously by means of SLR, hence providing a possible approach to track the evolution of orbit due to GWs. Historically, the data of SLR have been

* xupeng@imech.ac.cn

employed in various scientific researches [34–37]. On the other hand, detecting GWs with SLR has an outstanding advantage that it requires no further investment to any new and advanced facilities, and the only cost is a thorough analysis of data. Besides, the joint detection with multiple satellites and the future development of SLR technology will both improve the performance of this method. The orbital frequencies of most laser-ranged satellites resides in the 10^{-5} - 10^{-4} Hz range, which is another reason for our choice of the target frequencies.

The aim of our study is to investigate the feasibility and prospect of GW detection via SLR, in the circumstance where orbital resonance takes place. To this end, on the basis of previous study [26, 38–42], we adjust the equations of orbital perturbation to describe the resonance induced by individual GW signal, hence allowing numerical and analytical calculations of the osculate orbital elements. These expressions are then applied to the analysis of GW-induced resonance and its dependence on relevant parameters. Finally, our method is tested on two types of sources, which are SMBHBs and Milky Way DWDs.

II. FORMALISM

The phenomenon of orbital resonance can be described by the equations of motion (EoM) of the osculating orbital elements, with GWs acting as small perturbations. To begin with, we introduce a cylindrical coordinate $\{\mathbf{r}, \boldsymbol{\theta}, \mathbf{l}\}$ whose origin is placed at the test binary's center of mass, and $\{\mathbf{r}, \boldsymbol{\theta}\}$ represent the bases of polar coordinates within the orbital plane, \mathbf{l} being the unit vector perpendicular to them. The unperturbed Keplerian motion is characterized by six constants $\mathbf{X} = \{P, e, I, \Omega, \omega, \varepsilon\}$, including the orbital period, eccentricity, inclination, longitude of ascending node, argument of pericenter, and the compensated mean anomaly, respectively.

The separation of a test binary $r(t; \mathbf{X})$ follows the Kepler's equations

$$r(t; \mathbf{X}) = a [1 - e \cos E(t)], \quad (1)$$

$$E(t) - e \sin E(t) = \frac{2\pi t}{P} + \varepsilon, \quad (2)$$

$$\psi(t) = 2 \arctan \left[\sqrt{\frac{1+e}{1-e}} \tan \frac{E(t)}{2} \right], \quad (3)$$

where the true anomaly ψ is the angle measured counterclockwise from the pericenter, and E represents the eccentric anomaly.

With incident GWs, Eq.(1-3) are still valid under the condition that \mathbf{X} are regarded as the osculating orbital elements that satisfy the following the EoM [26, 38–42]:

$$\begin{aligned} \dot{\mathbf{X}} &= \boldsymbol{\Gamma}(\mathbf{X}, \psi, \hat{\mathbf{n}}_{\text{GW}}, t), \\ \boldsymbol{\Gamma} &\equiv \mathbf{T}^A(\mathbf{X}, \psi, \hat{\mathbf{n}}_{\text{GW}}) \ddot{h}_A(\hat{\mathbf{n}}_{\text{GW}}, t). \end{aligned} \quad (4)$$

The GW-induced perturbations $\boldsymbol{\Gamma}$ depend on the 6 elements \mathbf{X} , and $\psi, \hat{\mathbf{n}}_{\text{GW}}, t$. $\hat{\mathbf{n}}_{\text{GW}} = \hat{\mathbf{n}}_{\text{GW}}(\vartheta, \phi)$ denotes the

direction of source, and \mathbf{T}^A the transfer functions corresponding to the GW polarization A ($A = +, \times$). In the following we will introduce the methods of solving Eq.(4) numerically, and an analytical solution is acquired under several simplifications.

A. Numerical Solution

The transfer functions $\mathbf{T}^A(\mathbf{X}, \psi, \hat{\mathbf{n}}_{\text{GW}})$ give the couplings between the orbital elements \mathbf{X} and the incident GW h_A . In this paper, our main concern is the perturbation of the orbital period P (or the semi-major axis a), which is directly related to the total energy of the test binary. The transfer function for P reads [26].

$$T_P^A = \frac{3P^2\gamma}{4\pi} \left(\frac{e \sin \psi}{1 + e \cos \psi} \hat{r}^i + \hat{\theta}^i \right) \hat{r}^j e_{ij}^A, \quad (5)$$

where we have defined $\gamma = \sqrt{1 - e^2}$. e_{ij}^A are the polarization tensors of GW, and $\hat{r}^i, \hat{\theta}^i$ are the unit vectors of $\mathbf{r}, \boldsymbol{\theta}$, respectively. The explicit forms of other transfer functions and the coefficients of e_{ij}^A in the test binary frame can also be found in Ref. [26].

The above EoM of \mathbf{X} are not closed until we include the time derivative of ψ , following Refs. [38, 42] we have

$$\begin{aligned} \dot{\psi} &= \frac{\ell}{r^2} - \dot{\omega} - \dot{\Omega} \cos I \\ &= \frac{2\pi}{P} \frac{(1 + e \cos \psi)^2}{\gamma^3} - \dot{\omega} - \dot{\Omega} \cos I, \end{aligned} \quad (6)$$

ℓ being the total angular momentum of the test binary in unit of the reduced mass. Eq.(4) and Eq.(6) form a system of ODES for $\{\mathbf{X}, \psi\}$, which can be solved numerically. Without loss of generality, we further set $\psi = 0$ at $t = 0$, meaning that the binary is initially at its pericenter. As a result, the initial conditions (IC) are $\{\psi, \mathbf{X}\} = \{0, \mathbf{X}_0\}$ at $t = 0$.

B. Analytical Solution

To understand the resonant behavior qualitatively, we also derive the analytical solution under the simplifications that the orbit of test binary is circular and the incident GW is modeled as a monochromatic wave with redshifted frequency f_{GW} and initial phase φ_{GW} .

At the resonance frequency $f_{\text{GW}} = f_{\text{res}} \equiv 2/P$, the variation of P is dominated by a linear (i.e. resonant) term, and this effect will accumulate in time. The secular perturbation of P , defined as \dot{P} averaged over one revolution, reads

$$\begin{aligned} \dot{P}_{\text{sec}} &= 6\pi[(B - C) \sin(\varphi_{\text{GW}} - 2\omega) \\ &\quad - (A + D) \cos(\varphi_{\text{GW}} - 2\omega)], \end{aligned} \quad (7)$$

where A, B, C, D are constants determined by the incident GW. The detailed derivation can be found in Appendix A. Depending on the relative phase and direction

TABLE I. Parameters of LAGEOS2 (**L2**) and SDSSJ1430 + 2303 (**TS**).

Satellite		SMBHB	
P_0	13349 s	M_{bh}	$4 \times 10^7 M_\odot$
e_0	0.0135	z	0.08105
I_0	52.64°	ι	$\pi/6$
Ω_0	$\pi/3$	ϑ	$\pi/6$
ω_0	0	ϕ	0
ε_0	0	φ_{ref}	$\pi/4$

between the GW source and test binary, \dot{P}_{sec} can be either positive or minus. This expression provides an intuitive demonstration of orbital resonance, and in the case of Milky Way DWD detection, they can be used to make an order-of-magnitude analysis.

III. AN EXAMPLE OF GW-INDUCED ORBITAL RESONANCE

With numerical approach, the resonantly perturbed orbital elements in a specific case are calculated and analyzed in this section. Among all the candidates for the test binary, we take the laser ranging mission LAGEOS 2 [33, 36, 43] (**L2** for short) as an example, since it has relatively large eccentricity (0.0135) compared to LAGEOS (0.0045) and LARES (0.0008), thus can be more representative for general cases with slightly eccentric orbits. As for the incident signal, we are particularly interested in the GW sources like the SMBHB SDSSJ1430+2303 discovered via optical and X-ray observations [44], which will be referred to as the representative Target Source in the rest of this paper (**TS** for short).

Relevant parameters are listed in Tab. I, where the initial values of P, e, I for **L2** are taken from Ref. [36], and ε is derived from the IC. Ref. [44] reported the properties of the **TS** that constrained by EM observations. Here we simply assume that it consists of two black holes (BHs) with equal masses $M_{bh} = 4 \times 10^7 M_\odot$, and redshift $z = 0.08105$. Other parameters are randomly selected, since parameters such as Ω and ω change in time, and we are interested in a family of SMBHBs with properties similar to SDSSJ1430+2303 rather than this specific one. Moreover, a detailed discussion on the parameter space is given in Appendix B.

As for the modelling of GW, we adopt the SEOBNR time-domain waveform provided by the open-source code LALSuite [45], and set the reference frequency $f_{\text{ref}} = 3\text{mHz}$, following the convention of LISA Data Challenge [46]. The orbital phase of source at f_{ref} is denoted as φ_{ref} , which we set to $\varphi_{\text{ref}} = \pi/4$.

Roughly speaking, the inspiral stage of GW ends when

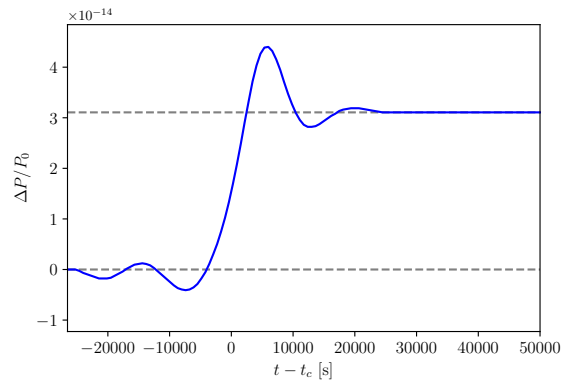


FIG. 1. The relative variation of P under chirping GW signal. t_c stands for the time when the waveform of coalescence arrives at the satellite.

f_{GW} equals the frequency of the innermost stable circular orbit $f_{\text{ISO}} \equiv 1/(6^{3/2}\pi M)$, where M denotes the total mass of the source. For the case under consideration, $f_{\text{res}} > f_{\text{ISO}}$, indicating that resonance happens mainly during the merger stage. As is shown in Fig. 1, P exhibits linear growth for $\sim 10^4$ s, and finally reaches a steady relative difference $\Delta P_{\text{fin}}/P_0 = 3.107 \times 10^{-14}$, equivalent to the variation in semi-major axis

$$\Delta a_{\text{fin}} \approx \frac{2a}{3P} \Delta P_{\text{fin}} = 2.519 \times 10^{-7} \text{ m}. \quad (8)$$

This example offers a first glance to the phenomenon of GW-induced resonance. Other examples where resonance starts at the inspiral stage can be found in Fig. 6 of Appendix B.

IV. GW DETECTION WITH ORBITAL RESONANCE

The effect of orbital resonance can accumulate in time, thus may eventually enter the scope of detection. Meanwhile, SLR provides continuous and precise measurement of the satellite's orbit. In this section, we will explore and quantify the feasibility of detecting GWs with SLR.

As is mentioned previously, SMBHBs are among the strongest sources in the 10^{-5} to 10^{-4} Hz band, and LISA is expected to observe a few SMBHBs per year (conservative estimation), thus we will treat them as individual sources. On the contrary, the population of solar mass compact binaries in the Milky Way, which is dominated by DWDs, are large in amount. The combined signals of tens of millions of unresolvable systems form a stochastic GW foreground at frequencies below a few mHz [29–32]. This foreground can be detected by space-based interferometers such as LISA [29, 30, 47–49], Taiji [7, 8] and TianQin [50]. Given that their orbits are slow-varying, one may naturally wonder that whether DWDs with specific frequencies can be picked out from

the foreground through the long-term resonant interactions with the SLR satellites.

A. SMBHB

SLR is a precision probe of orbital motion. Collecting the round-trip times of laser pulses allows one to track the “normal point” distances over time. With the help of the precise orbit determination program GEODYN [51], the orbital elements of satellites can be calculated based on a number of distance measurements. In the most optimistic case for **L2** and **TS** (i.e. $\{\vartheta, \phi, \iota, \varphi_{\text{ref}}, \omega\}$ are set to the **OP** defined in Appendix B), $\Delta a_{\text{fin}} = 5.047 \times 10^{-7}$ m. While, current precision of SLR distance measurement is at the mm level [34], thus it seems difficult to identify such tiny variation in a out of uncertainty.

The orbital elements only characterize the motion of the satellite in an average sense. Details of the orbital motion should be described with other quantities. In this paper, we adopt the residual distance $\delta r(t) \equiv r(t; \mathbf{X}) - r(t; \mathbf{X}_0)$ calculated via Eq.(1-3) as an observable, and try to reveal the signature of GW with the matched filtering technique.

Shown in Fig. 2 is the most optimistic response of **L2** to **TS** in terms of $\delta r(t)$. During the time span of resonance ($t \in (0.2, 0.4)$ day), the central values of δr grow in time, and finally reach a steady value $\bar{\delta r}_{\text{fin}} = 5 \times 10^{-7}$ m $\approx \Delta a_{\text{fin}}$. Afterwards, δr oscillates around $\bar{\delta r}_{\text{fin}}$ with increasing amplitude. This pro-resonance residual is nothing but the difference between two unperturbed elliptic Kepler orbits with slightly different orbital elements. Trivial as it may seem, this pattern is the consequence of secular evolution, and it is absent in the case of non-resonance interactions with GW. Therefore, once δr is observed to vary similarly to Fig. 2, it would at least indicate GW-induced resonance as a possible cause. Next, we will estimate whether the growth of δr in the resonance stage, together with this pro-resonance pattern, can be used to detect GW signal.

To quantify the observational evidence of GW-induced resonance, we adopt the SNR of matched filtering derived in Appendix C, which depends on the SLR uncertainty σ . Following Ref. [27], two values of σ are considered:

- a. current precision: $\sigma = 3$ mm, 50,000 normal point measurements per year;
- b. improved precision: $\sigma = 0.3$ mm, 200,000 measurements per year.

For the optimistic case shown in Fig. 2, the resonance stage contributes only 5×10^{-4} for the current precision or 1×10^{-2} for the improved precision to the total SNR. In the pro-resonance stage, when the timescale is much smaller than $P^2/\Delta P_{\text{fin}}$, the magnitude of δr grows linearly with time. As a result, the relationship between SNR and T_{obs} can be approximated as a power-law function (see Appendix C). In Fig. 3 we have plotted SNR

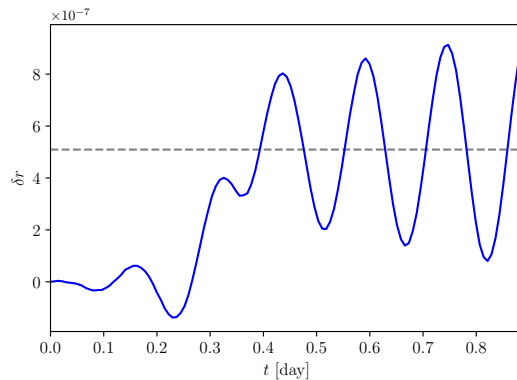


FIG. 2. The residual distance of **L2** under the influence of incident GW from **TS** in the most optimistic case. The mean value of δr after resonance is 5×10^{-7} m.

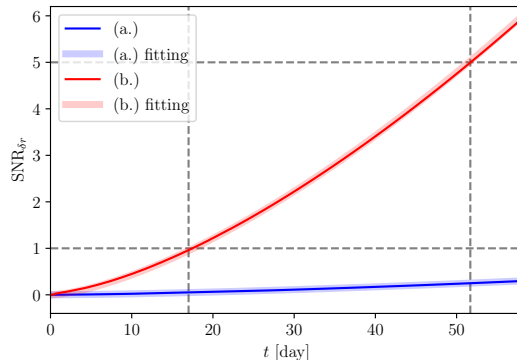


FIG. 3. SNR as functions of observation time under precision a (blue curves) and precision b (red curves). The thin curves are obtained from numerical calculation, while thick ones are the power-law fitting functions.

against T_{obs} under different laser ranging precision, obtained by means of numerical calculations and the power-law fitting functions. As is shown, $\text{SNR} > 1$ can be achieved when $T_{\text{obs}} > 130$ days (current precision) or 17 days (improved precision). Besides, if we set the threshold for GW detection to $\text{SNR} = 5$, $T_{\text{obs}} > 51$ days is required for precision b, and precision a would require an unrealistic long time.

According to the discussion in Appendix B, the resonant response of orbit also depends on the masses and distance (or redshift) of GW source, which inspires us to go beyond **TS** and look for more promising sources. Given that the nearest SMBHB system reported so far located in NGC 7277, with redshift 0.006 and component masses $1.54 \times 10^8 M_{\odot}$ and $6.3 \times 10^6 M_{\odot}$ [52], the existence of SMBHB at redshift around $z \sim 0.01$ can not be ruled out. Suppose that **L2** is in resonant interaction with the GW from a SMBHB with redshift $z = 0.01$ and equal component masses $M_{\text{bh}} = 5.8 \times 10^7 M_{\odot}$ (corresponding to the peak of the red curve in Fig. 7), in

the most optimistic case, $\text{SNR} = 5$ can be achieved after an observation time of 74 days (current precision) or 10 days (improved precision). Furthermore, for an imaginary SMBHB at $z = 0.001$, by only taking the data within resonance stage into consideration, the most optimistic SNR is 0.15 (current precision) or 3 (improved precision).

In addition, there are other factors which may improve the prospect of this method, such as increasing the semi-major to, e.g. 4×10^4 km (see Appendix B3). Besides, using **L2** alone may lead to a conservative estimate, since incident GW can also leave imprints on other laser-ranged satellites. Assuming that the uncertainties of different satellites are uncorrelated, the total SNR scales as the square root of the number of **L2**-like satellites, and it can be further improved with the inclusion of high orbit satellites such as Etalon [53]. We will leave the quantitative analysis of joint detection with multiple satellites to further research.

Strictly speaking, the application of our method requires that other gravitational or non-gravitational perturbations are precisely modeled and accounted. A wide variety of perturbations have been investigated in the literature, such as geopotentials harmonics [54, 55], atmospheric drag [56, 57], thermal-thrust effects [58], Solar radiation pressure, dynamic solid tide and ocean tide [59, 60], etc. Currently, the precision of SLR's application in scientific problems is mainly limited by the unmodeled or mismodeled factors, thus the prospect of our method would increase with the understanding towards them.

The data of SLR can be interpreted in multiple ways. Except for δr , the residual acceleration δa is also employed in a wide range of literature [34, 57, 60–62]. As an example, we consider the radial component of acceleration, and its residual δa_r oscillates around $-2.286 \times 10^{-13} \text{m/s}^2$ in the pro-resonance stage. It is reported in Refs. [61, 62] that after modelling the known perturbations, the residual mean acceleration away from geodesic motion for LARES (or the two LAGEOS satellites) is less than $0.5 \times 10^{-12} \text{m/s}^2$ (or $1-2 \times 10^{-12} \text{m/s}^2$). With these estimations, we expect that the measurements of δa_r may also help to identify GW signals.

In summary, the results of this section show that the resonant effect of a single signal may not be remarkable, but it has the potential to reveal the first GW signal from SMBHB in the 10^{-5} - 10^{-4} Hz range, during the absence of space-based detectors.

B. Milky Way DWD Foreground

Considering that the typical timescale on which DWDs evolve ($> \text{Myr}$) is much greater than the operating times of any satellite, GW from such sources can be approximately treated as monochromatic sources [47]. To make an order-of-magnitude estimate, we employ the simplified expression in Eq.(7), and average over the position,

orientation and phase of sources $\{\vartheta, \phi, \iota, \varphi_{\text{GW}}\}$, as well as the inclination of the satellite orbit I .

Since \dot{P} can be either positive or negative, averaging over an ensemble of stochastic GWs would yield a vanishing difference in P . To find the observable signature of GWs, we should compute the root-mean-square (RMS) value. The expression of ΔP_{RMS} for a single source is derived in Appendix A. As for the DWD foreground, the variance of ΔP should be added over sources with GW frequencies near f_{res} :

$$\begin{aligned} \Delta P_{\text{RMS}}^2 &= \left(\frac{12}{5} \pi T_{\text{obs}} \right)^2 H_{\text{RMS}}^2(f_{\text{res}}) \Delta N(f_{\text{res}}, \Delta f_{\text{obs}}) \\ &\approx \left(\frac{12}{5} \pi \right)^2 H_{\text{RMS}}^2(f_{\text{res}}) \frac{dN}{df}(f_{\text{res}}) T_{\text{obs}}, \end{aligned} \quad (9)$$

where $H_{\text{RMS}}(f_{\text{res}})$ and $\Delta N(f_{\text{res}}, \Delta f_{\text{obs}})$ are the RMS amplitude (averaged over sources) and the number of sources in the $(f_{\text{res}} - \Delta f_{\text{obs}}/2, f_{\text{res}} + \Delta f_{\text{obs}}/2)$ range, and $\Delta f_{\text{obs}} \equiv 1/T_{\text{obs}}$, T_{obs} being the observation time.

The amplitude of DWD foreground can be estimated according to the galactic confusion noise S_c of LISA (given in the form of sky averaged sensitivity) [63–65]:

$$\begin{aligned} S_c(f) &= \frac{2}{5} H_{\text{RMS}}^2(f) \Delta N(f, \Delta f_{\text{LISA}}) T_{\text{LISA}} \\ &\approx \frac{2}{5} H_{\text{RMS}}^2(f) \frac{dN}{df}(f), \end{aligned} \quad (10)$$

where T_{LISA} represents the operating time of LISA, and again $\Delta f_{\text{LISA}} \equiv 1/T_{\text{LISA}}$. The fitting form in Ref. [65] gives $S_c(f_{\text{res}}) = 1.079 \times 10^{-35} \text{Hz}^{-1}$ for $T_{\text{LISA}} = 4$ years. Combining Eq.(9) and Eq.(10), one has

$$\Delta P_{\text{RMS}} \approx 6\pi \sqrt{\frac{2}{5} S_c(f_{\text{res}}) T_{\text{obs}}}. \quad (11)$$

That is, on average, the orbital period varies with time as $\sqrt{T_{\text{obs}}}$, as is expected for a Brownian random walk. For **L2**, even with 15 years of data collection, $\Delta P_{\text{RMS}} \approx 8 \times 10^{-13} \text{s}$, $\Delta a_{\text{RMS}} \approx 5 \times 10^{-10} \text{m}$, which is lower than the effect of a single SMBHB event by 2-3 orders of magnitude, and can be easily hidden in the uncertainty of measurement (assumed in Sec. IV A). Therefore, we can hardly expect SLR to serve as a probe of Milky Way DWD foreground.

V. CONCLUSION

During the absence of space-based detectors, SLR may be the only ready-to-use approach of GW detection in the 10^{-5} - 10^{-4} Hz range, especially to the detection of SMBHB mergers. The aim of this paper is to investigate the feasibility of detecting GWs through their resonant interactions with laser-ranged satellites. To this end, both numerical and analytical methods were adopted to calculate the responses of satellite orbits to incident

GWs, and the dependence on relevant parameters was also analyzed.

In the scope of our research, we take the GW emitted by SMBHB SDSSJ1430+2303 (**TS**) and laser-ranged satellite LAGEOS 2 (**L2**) as an example, and the results can be easily generated to similar sources and SLR missions. By assuming two sets of precisions, we calculated the optimal matched filtering SNR in terms of the SLR distance residual. In the most optimistic case, $\text{SNR} > 1$ can be achieved when $T_{\text{obs}} > 130$ days (current precision) or 17 days (improved precision). Besides, if we set the threshold for GW detection to $\text{SNR} = 5$, 51 days is required for the improved precision, while current precision would require an unrealistic long time.

This method performs better for sources at lower redshifts. If we go beyond the **TS** and assume a SMBHB located at $z = 0.01$, $\text{SNR} = 5$ can be achieved after an observation time of 74 days (current precision) or 10 days (improved precision). Other factors may as well enhance

its performance, such as increasing the semi-major axis of satellite, and considering the joint detection with multiple satellites. While, as for the DWD foreground, its impact on SLR missions is much weaker than a single SMBHB, thus we can hardly expect SLR to serve as a probe of this foreground.

In addition, the prospect of our method also improves the understandings of the residual orbital perturbations for SLR missions.

In summary, owing to the long-term data collection and comprehensive future development of SLR, the resonance of laser-ranged satellite may not be quite remarkable, but it has the potential to reveal the first GW from SMBHB, during the absence of space-based detectors. Meanwhile, GW detection with SLR is an economical approach in the sense that it requires no further investment to any new and advanced facilities, and the only cost is a thorough analysis of data.

-
- [1] B. P. Abbott, R. Abbott, T. D. Abbott, *et al.* (LIGO Scientific Collaboration and Virgo Collaboration), Gw150914: The advanced ligo detectors in the era of first discoveries, *Phys. Rev. Lett.* **116**, 131103 (2016).
- [2] J. Aasi *et al.* (LIGO Scientific), Advanced LIGO, *Class. Quant. Grav.* **32**, 074001 (2015), [arXiv:1411.4547 \[gr-qc\]](#).
- [3] R. Abbott *et al.* (LIGO Scientific, Virgo), GWTC-2: Compact Binary Coalescences Observed by LIGO and Virgo During the First Half of the Third Observing Run, *Phys. Rev. X* **11**, 021053 (2021), [arXiv:2010.14527 \[gr-qc\]](#).
- [4] R. Abbott, T. D. Abbott, F. Acernese, *et al.*, GWTC-3: Compact Binary Coalescences Observed by LIGO and Virgo During the Second Part of the Third Observing Run, *arXiv e-prints*, [arXiv:2111.03606 \(2021\)](#), [arXiv:2111.03606 \[gr-qc\]](#).
- [5] P. Amaro-Seoane, H. Audley, S. Babak, *et al.*, Laser Interferometer Space Antenna, *arXiv e-prints*, [arXiv:1702.00786 \(2017\)](#), [arXiv:1702.00786 \[astro-ph.IM\]](#).
- [6] W. rui Hu and Y.-L. Wu, The taiji program in space for gravitational wave physics and the nature of gravity, *National Science Review* **4**, 685 (2017).
- [7] Z. Luo, Y. Wang, Y. Wu, W. Hu, and G. Jin, The Taiji program: A concise overview, *Progress of Theoretical and Experimental Physics* **2021**, 10.1093/ptep/ptaa083 (2020), 05A108, <https://academic.oup.com/ptep/article-pdf/2021/5/05A108/37953044/ptaa083.pdf>.
- [8] Z. Luo, Z. Guo, G. Jin, Y. Wu, and W. Hu, A brief analysis to taiji: Science and technology, *Results in Physics* **16**, 102918 (2020).
- [9] W.-H. Ruan, Z.-K. Guo, R.-G. Cai, and Y.-Z. Zhang, Taiji Program: Gravitational-Wave Sources, *arXiv e-prints*, [arXiv:1807.09495 \(2018\)](#), [arXiv:1807.09495 \[gr-qc\]](#).
- [10] J. Luo *et al.* (TianQin), TianQin: a space-borne gravitational wave detector, *Class. Quant. Grav.* **33**, 035010 (2016), [arXiv:1512.02076 \[astro-ph.IM\]](#).
- [11] P. D. Lasky *et al.*, Gravitational-wave cosmology across 29 decades in frequency, *Phys. Rev. X* **6**, 011035 (2016), [arXiv:1511.05994 \[astro-ph.CO\]](#).
- [12] Z. Arzoumanian *et al.* (NANOGrav), The NANOGrav 12.5 yr Data Set: Search for an Isotropic Stochastic Gravitational-wave Background, *Astrophys. J. Lett.* **905**, L34 (2020), [arXiv:2009.04496 \[astro-ph.HE\]](#).
- [13] G. Janssen *et al.*, Gravitational wave astronomy with the SKA, *PoS AASKA14*, 037 (2015), [arXiv:1501.00127 \[astro-ph.IM\]](#).
- [14] B. Mashhoon, On tidal resonance., *Astrophys. J.* **223**, 285 (1978).
- [15] B. Mashhoon, B. J. Carr, and B. L. Hu, The influence of cosmological gravitational waves on a Newtonian binary system, *Astrophys. J.* **246**, 569 (1981).
- [16] C. Chicone, B. Mashhoon, and D. G. Retzliff, Gravitational ionization: Periodic orbits of binary systems perturbed by gravitational radiation, *Ann. Inst. H. Poincaré Phys. Theor.* **64**, 87 (1996), [arXiv:gr-qc/9508065](#).
- [17] C. Chicone, B. Mashhoon, and D. G. Retzliff, On the ionization of a Keplerian binary system by periodic gravitational radiation, *J. Math. Phys.* **37**, 3997 (1996), [Erratum: *J. Math. Phys.* **38**, 544 (1997)], [arXiv:gr-qc/9605031](#).
- [18] C. Chicone, B. Mashhoon, and D. G. Retzliff, Sustained resonance: A Binary system perturbed by gravitational radiation, *J. Phys. A* **33**, 513 (2000), [arXiv:gr-qc/9911123](#).
- [19] L. Hui, S. T. McWilliams, and I.-S. Yang, Binary systems as resonance detectors for gravitational waves, *Phys. Rev. D* **87**, 084009 (2013).
- [20] L. Iorio, Orbital effects of a monochromatic plane gravitational wave with ultra-low frequency incident on a gravitationally bound two-body system, *ScienceOpen Research* **2014**, 1 (2014), [arXiv:1104.4853 \[gr-qc\]](#).
- [21] D. Blas, D. L. Nacir, and S. Sibiriyakov, Ultralight dark matter resonates with binary pulsars, *Phys. Rev. Lett.* **118**, 261102 (2017).
- [22] V. Desjacques, E. Grishin, and Y. B. Ginat, Axion oscillations in binary systems: angle-action surgery, *Astrophys. J.* **901**, 85 (2020), [arXiv:2003.10552 \[gr-qc\]](#).

- [23] J. M. Armaleo, D. López Nacir, and F. R. Urban, Pulsar timing array constraints on spin-2 ULDM, *JCAP* **09**, 031, [arXiv:2005.03731 \[astro-ph.CO\]](https://arxiv.org/abs/2005.03731).
- [24] D. Blas, D. López Nacir, and S. Sibiryakov, Secular effects of ultralight dark matter on binary pulsars, *Phys. Rev. D* **101**, 063016 (2020), [arXiv:1910.08544 \[gr-qc\]](https://arxiv.org/abs/1910.08544).
- [25] L. Iorio and M. L. Ruggiero, Perturbations of the orbital elements due to the magnetic-like part of the field of a plane gravitational wave, *Int. J. Mod. Phys. D* **30**, 2150088 (2021), [arXiv:2106.14462 \[gr-qc\]](https://arxiv.org/abs/2106.14462).
- [26] D. Blas and A. C. Jenkins, Detecting stochastic gravitational waves with binary resonance, *Phys. Rev. D* **105**, 064021 (2022).
- [27] D. Blas and A. C. Jenkins, Bridging the μHz Gap in the Gravitational-Wave Landscape with Binary Resonances, *Phys. Rev. Lett.* **128**, 101103 (2022), [arXiv:2107.04601 \[astro-ph.CO\]](https://arxiv.org/abs/2107.04601).
- [28] A. Klein, E. Barausse, A. Sesana, A. Petiteau, E. Berti, S. Babak, J. Gair, S. Aoudia, I. Hinder, F. Ohme, and B. Wardell, Science with the space-based interferometer elisa: Supermassive black hole binaries, *Phys. Rev. D* **93**, 024003 (2016).
- [29] S. Yu and C. S. Jeffery, The gravitational wave signal from diverse populations of double white dwarf binaries in the Galaxy, *Astron. Astrophys.* **521**, A85 (2010), [arXiv:1007.4267 \[astro-ph.SR\]](https://arxiv.org/abs/1007.4267).
- [30] A. J. Ruiter, K. Belczynski, M. Benacquista, S. L. Larson, and G. Williams, The lisa gravitational wave foreground: A study of double white dwarfs, *The Astrophysical Journal* **717**, 1006 (2010).
- [31] G. Nelemans, L. R. Yungelson, and S. F. Portegies Zwart, The gravitational wave signal from the Galactic disk population of binaries containing two compact objects, *Astron. Astrophys.* **375**, 890 (2001), [arXiv:astro-ph/0105221 \[astro-ph\]](https://arxiv.org/abs/astro-ph/0105221).
- [32] G. Nelemans, L. R. Yungelson, S. F. Portegies Zwart, and F. Verbunt, Population synthesis for double white dwarfs I. close detached systems, *Astron. Astrophys.* **365**, 491 (2001), [arXiv:astro-ph/0010457](https://arxiv.org/abs/astro-ph/0010457).
- [33] Ilrs, international laser ranging service: LAGEOS-2, https://ilrs.gsfc.nasa.gov/missions/satellite_missions/current_missions/lag2_general.html.
- [34] I. Ciufolini, R. Matzner, A. Paolozzi, E. C. Pavlis, G. Sindoni, J. Ries, V. Gurzadyan, and R. Koenig, Satellite Laser-Ranging as a Probe of Fundamental Physics, *Scientific Reports* **9**, 15881 (2019), [arXiv:1907.00395 \[gr-qc\]](https://arxiv.org/abs/1907.00395).
- [35] L. Iorio, Does Newton's gravitational constant vary sinusoidally with time? Orbital motions say no, *Classical and Quantum Gravity* **33**, 045004 (2016), [arXiv:1504.07233 \[gr-qc\]](https://arxiv.org/abs/1504.07233).
- [36] I. Ciufolini *et al.*, A test of general relativity using the LARES and LAGEOS satellites and a GRACE Earth gravity model, *Eur. Phys. J. C* **76**, 120 (2016), [arXiv:1603.09674 \[gr-qc\]](https://arxiv.org/abs/1603.09674).
- [37] I. Ciufolini, A. Paolozzi, E. C. Pavlis, G. Sindoni, J. Ries, R. Matzner, R. Koenig, C. Paris, V. Gurzadyan, and R. Penrose, An Improved Test of the General Relativistic Effect of Frame-Dragging Using the LARES and LAGEOS Satellites, *Eur. Phys. J. C* **79**, 872 (2019), [arXiv:1910.09908 \[gr-qc\]](https://arxiv.org/abs/1910.09908).
- [38] D. Brouwer and G. M. Clemence, *Methods of celestial mechanics* (1961).
- [39] J. A. Burns, Elementary derivation of the perturbation equations of celestial mechanics, *American Journal of Physics* **44**, 944 (1976), <https://doi.org/10.1119/1.10237>.
- [40] C. D. Murray and S. F. Dermott, *Solar System Dynamics* (Cambridge University Press, 2000).
- [41] M. S. Turner, Influence of a weak gravitational wave on a bound system of two point-masses., *Astrophys. J.* **233**, 685 (1979).
- [42] W. M. Smart, *Celestial mechanics*, London: Longmans (1960).
- [43] M. Pearlman, D. Arnold, M. Davis, F. Barlier, R. Biancale, V. Vasiliev, I. Ciufolini, A. Paolozzi, E. Pavlis, K. Sońnica, and M. Bloßfeld, Laser geodetic satellites: a high-accuracy scientific tool, *Journal of Geodesy* **93** (2019).
- [44] N. Jiang, H. Yang, T. Wang, J. Zhu, Z. Lyu, L. Dou, Y. Wang, J. Wang, Z. Pan, H. Liu, X. Shu, and Z. Zheng, Tick-Tock: The Imminent Merger of a Supermassive Black Hole Binary, [arXiv e-prints](https://arxiv.org/abs/2201.11633), [arXiv:2201.11633 \[astro-ph.HE\]](https://arxiv.org/abs/2201.11633).
- [45] LIGO Scientific Collaboration, *LIGO Algorithm Library - LALSuite*, free software (GPL) (2018).
- [46] LISA data challenges., <https://lisa-1dc.1a1.in2p3.fr/>.
- [47] V. Korol, E. M. Rossi, P. J. Groot, G. Nelemans, S. Toonen, and A. G. A. Brown, Prospects for detection of detached double white dwarf binaries with Gaia, LSST and LISA, *Monthly Notices of the Royal Astronomical Society* **470**, 1894 (2017), <https://academic.oup.com/mnras/article-pdf/470/2/1894/18139327/stx1285.pdf>.
- [48] V. Korol, E. M. Rossi, and E. Barausse, A multimessenger study of the Milky Way's stellar disc and bulge with LISA, Gaia, and LSST, *Monthly Notices of the Royal Astronomical Society* **483**, 5518 (2018), <https://academic.oup.com/mnras/article-pdf/483/4/5518/27496911/sty3440.pdf>.
- [49] S. E. Timpano, L. J. Rubbo, and N. J. Cornish, Characterizing the galactic gravitational wave background with lisa, *Phys. Rev. D* **73**, 122001 (2006).
- [50] S.-J. Huang, Y.-M. Hu, V. Korol, P.-C. Li, Z.-C. Liang, Y. Lu, H.-T. Wang, S. Yu, and J. Mei, Science with the tianqin observatory: Preliminary results on galactic double white dwarf binaries, *Phys. Rev. D* **102**, 063021 (2020).
- [51] Geodyn documentation, <https://earth.gsfc.nasa.gov/index.php/geo/data/geodyn-documentation>.
- [52] Vögel, Karina T., Seth, Anil C., Baumgardt, Holger, Husemann, Bernd, Neumayer, Nadine, Hilker, Michael, Pechetti, Renuka, Mieske, Steffen, Dumont, Antoine, and Georgiev, Iskren, First direct dynamical detection of a dual supermassive black hole system at sub-kiloparsec separation, *Astron. Astrophys.* **658**, A152 (2022).
- [53] Gunter's space page. Etalon 1, 2., http://space.skyrocket.de/doc_sdat/etalon.htm.
- [54] I. Ciufolini *et al.*, A new laser-ranged satellite for General Relativity and space geodesy: I. An introduction to the LARES2 space experiment, *Eur. Phys. J. Plus* **132**, 336 (2017), [arXiv:1910.13818 \[gr-qc\]](https://arxiv.org/abs/1910.13818).
- [55] I. Ciufolini, E. C. Pavlis, G. Sindoni, J. C. Ries, A. Paolozzi, R. Matzner, R. Koenig, and C. Paris, A new laser-ranged satellite for General Relativity and space geodesy: II. Monte Carlo simulations and covariance analyses of the LARES 2 experiment, *Eur. Phys. J. Plus* **132**, 337 (2017), [arXiv:1911.06183 \[gr-qc\]](https://arxiv.org/abs/1911.06183).
- [56] L. Iorio, On the impact of the atmospheric drag on the

- LARES mission, *Acta Phys. Polon. B* **41**, 753 (2010), [arXiv:0809.3564 \[gr-qc\]](#).
- [57] C. Pardini, L. Anselmo, D. Massimo Lucchesi, and R. Peron, Estimation of the Perturbing Accelerations Induced on the LARES Satellite by Neutral Atmosphere Drag, *arXiv e-prints*, [arXiv:1611.02514](#) (2016), [arXiv:1611.02514 \[gr-qc\]](#).
- [58] D. M. Lucchesi, E. C. Pavlis, I. Ciufolini, and R. Peron, The Yarkovsky-Schach Thermal Effect on Lageos Satellites and its Modelling, in *EGS - AGU - EUG Joint Assembly*, EGS - AGU - EUG Joint Assembly (2003) p. 7494.
- [59] A. Milani, A. M. Nobili, and P. Farinella, *Non-gravitational perturbations and satellite geodesy*. (1987).
- [60] D. M. Lucchesi, L. Anselmo, M. Bassan, C. Pardini, R. Peron, G. Pucacco, and M. Visco, Testing the gravitational interaction in the field of the earth via satellite laser ranging and the laser ranged satellites experiment (LARASE), *Classical and Quantum Gravity* **32**, 155012 (2015).
- [61] I. Ciufolini, A. Paolozzi, E. Pavlis, J. Ries, V. Gurzadyan, R. Koenig, R. Matzner, R. Penrose, and G. Sindoni, Testing General Relativity and gravitational physics using the LARES satellite, *Eur. Phys. J. Plus* **127**, 133 (2012), [arXiv:1211.1374 \[gr-qc\]](#).
- [62] I. Ciufolini, C. Paris, G. Sindoni, R. Penrose, V. Gurzadyan, R. Matzner, J. Ries, E. C. Pavlis, R. Koenig, and A. Paolozzi, Fundamental Physics and General Relativity with the LARES and LAGEOS satellites, *Nucl. Phys. B Proc. Suppl.* **243-244**, 180 (2013), [arXiv:1309.1699 \[gr-qc\]](#).
- [63] P. Amaro-Seoane, S. Aoudia, S. Babak, P. Binétruy, E. Berti, A. Bohé, C. Caprini, M. Colpi, N. J. Cornish, K. Danzmann, J.-F. Dufaux, J. Gair, O. Jennrich, P. Jetzer, A. Klein, R. N. Lang, A. Lobo, T. Littenberg, S. T. McWilliams, G. Nelemans, A. Petiteau, E. K. Porter, B. F. Schutz, A. Sesana, R. Stebbins, T. Sumner, M. Vallisneri, S. Vitale, M. Volonteri, and H. Ward, Low-frequency gravitational-wave science with eLISA/NGO, *Classical and Quantum Gravity* **29**, 124016 (2012).
- [64] N. Cornish and T. Robson, Galactic binary science with the new LISA design, *J. Phys. Conf. Ser.* **840**, 012024 (2017), [arXiv:1703.09858 \[astro-ph.IM\]](#).
- [65] T. Robson, N. J. Cornish, and C. Liu, The construction and use of LISA sensitivity curves, *Classical and Quantum Gravity* **36**, 105011 (2019).
- [66] I. Ciufolini, On the orbit of the LARES satellite, *arXiv e-prints*, [gr-qc/0609081](#) (2006), [arXiv:gr-qc/0609081 \[gr-qc\]](#).

Appendix A: Derivation of the simplified analytical solution

The analytical solution is obtained under the simplifications that the test binary's orbit is circular and the incident GW is modeled as a monochromatic wave:

$$\begin{aligned} h_+ &= H_+ \cos(2\pi f_{\text{GW}}t + \varphi_{\text{GW}}), \\ h_\times &= H_\times \sin(2\pi f_{\text{GW}}t + \varphi_{\text{GW}}), \end{aligned} \quad (\text{A1})$$

where f_{GW} and φ_{GW} are the redshifted frequency and initial phase, respectively. The amplitudes $H_{+/\times}$ can

be expressed in terms of the redshifted chirp mass \mathcal{M}_c , inclination of angular momentum ι , luminosity distance d_L and f_{GW} as

$$\begin{aligned} H_+ &= \frac{4\mathcal{M}_c^{5/3}(\pi f_{\text{GW}})^{2/3}}{d_L} \frac{1 + \cos^2 \iota}{2}, \\ H_\times &= \frac{4\mathcal{M}_c^{5/3}(\pi f_{\text{GW}})^{2/3}}{d_L} \cos \iota, \end{aligned} \quad (\text{A2})$$

Moreover, the orbital elements evolve much slower than the Keplerian motion, thus we simply assume that \mathbf{X} in the r.h.s of Eq.(4) are fixed to \mathbf{X}_0 . This is equivalent to expanding Eq.(4) in powers of the GW polarizations h_A , and keeping only the linear order. For example, substituting $P = P_0 + P_1(t; h_A) + \mathcal{O}(h_A^2)$ into Eq.(4, 5), and neglecting the $\mathcal{O}(h_A^2)$ and higher order terms, it follows that

$$\dot{P} = \frac{3P_0^2}{4\pi} e_{ij}^A \hat{\theta}^i \hat{r}^j \ddot{h}_A \quad (\text{A3})$$

for a circular orbit. In the rest of this appendix we will drop the subscript “0” for brevity, and one has to keep in mind that \mathbf{X} in the r.h.s. take the initial values.

We are mainly interested in the variation of P . From $t = 0$ to $t = t_f$, the difference in P reads

$$\begin{aligned} \Delta P &= -\frac{3\pi\alpha^2}{2} \int_0^{t_f} dt \\ &\times [(A - D) \cos(\Delta_+) + (A + D) \cos(\Delta_-) \\ &+ (B + C) \sin(\Delta_+) + (B - C) \sin(\Delta_-)], \end{aligned} \quad (\text{A4})$$

where the coefficients A, B, C, D are all constants:

$$\begin{aligned} A &= H_+ \left[-\frac{1}{2} \sin 2\vartheta \cos \varphi \sin I \right. \\ &\quad \left. + \frac{1}{2} (1 + \cos^2 \vartheta) \sin 2\varphi \cos I \right], \\ B &= H_+ \left[\frac{1}{2} \sin^2 \varphi - \frac{1}{2} \cos^2 \varphi \cos^2 I - \frac{1}{2} \cos^2 \vartheta \cos^2 \varphi \right. \\ &\quad \left. + \frac{1}{2} (\sin \vartheta \sin I - \cos \vartheta \sin \varphi \cos I)^2 \right] \\ C &= H_\times (\cos \vartheta \cos 2\varphi \cos I + \sin \vartheta \sin \varphi \sin I), \\ D &= H_\times \left[-\frac{1}{2} \sin \vartheta \cos \varphi \sin 2I \right. \\ &\quad \left. + \frac{1}{2} \cos \vartheta \sin 2\varphi (1 + \cos^2 I) \right], \end{aligned} \quad (\text{A5})$$

In these expressions we have defined $\alpha \equiv f_{\text{GW}}P$ and $\varphi \equiv \phi - \Omega$, and the time-dependence of the integrand originates from Δ_\pm :

$$\Delta_\pm \equiv (2 \pm \alpha) \frac{2\pi}{P} t + 2\omega \pm \varphi_{\text{GW}}. \quad (\text{A6})$$

Resonance occurs at frequency $f_{\text{res}} \equiv 2/P$ ($\alpha = 2$), where the variation of P is dominated by a term which

is linear in time. The secular perturbation of P , defined as \dot{P} averaged over one revolution, reads

$$\dot{P}_{\text{sec}} = 6\pi[(B - C)\sin(\varphi_{\text{GW}} - 2\omega) - (A + D)\cos(\varphi_{\text{GW}} - 2\omega)]. \quad (\text{A7})$$

A reasonable conclusion can be drawn from Eq.(A7) that $|\dot{P}_{\text{sec}}|$ is maximized when the orbital planes of the source binary and the test binary are face-on or face-off, i.e. $\{\vartheta = I, \phi = \Omega - \pi/2, \iota = 0\}$ or $\{\vartheta = \pi - I, \phi = \Omega + \pi/2, \iota = \pi\}$. In both cases,

$$\dot{P}_{\text{sec}} = 12\pi H \sin(\varphi_{\text{GW}} - 2\omega), \quad (\text{A8})$$

where $H \equiv 4\mathcal{M}_c^{5/3}(\pi f_{\text{GW}})^{2/3}d_L^{-1}$.

If we further average over the position, orientation and phase of sources $\{\vartheta, \phi, \iota, \varphi_{\text{GW}}\}$, as well as the inclination of the test orbit I , the remaining terms in the variance of \dot{P}_{sec} are

$$\langle \dot{P}_{\text{sec}}^2 \rangle = 18\pi^2 \langle A^2 + B^2 + C^2 + D^2 \rangle, \quad (\text{A9})$$

where

$$\begin{aligned} \langle A^2 \rangle &= \frac{11}{90} \langle H_+^2 \rangle, & \langle B^2 \rangle &= \frac{5}{18} \langle H_+^2 \rangle, \\ \langle C^2 \rangle &= \frac{5}{18} \langle H_\times^2 \rangle, & \langle D^2 \rangle &= \frac{11}{90} \langle H_\times^2 \rangle. \end{aligned} \quad (\text{A10})$$

Using $\langle H_+^2 \rangle = 7H^2/15$, $\langle H_\times^2 \rangle = H^2/3$, the RMS evolution of P after observation time T_{obs} is hence

$$\Delta P_{\text{RMS}} = \sqrt{\langle \dot{P}_{\text{sec}}^2 \rangle} T_{\text{obs}} = \frac{12}{5} \pi H T_{\text{obs}}. \quad (\text{A11})$$

Appendix B: Dependence on parameters

The resonant response of the test binary depends on several parameters, including the position, orientation, redshift, and component masses of the GW source, and the initial orbital elements of itself. For monochromatic sources, the relationship between orbital resonance and aforementioned parameters are well manifested by the formalism deduced in Appendix. A. In the case of chirp signal, to illustrate the impacts of parameters, we vary their values in turn while keeping others the same as Tab. I, and calculate the evolution of P (or a) numerically. For brevity, the subscript ‘‘0’’ of \mathbf{X}_0 is left out without confusion.

1. the celestial coordinate (ϑ, ϕ) of GW source

The role of inclination angle ι in GW amplitude is straightforward, i.e., it reaches the maximum at $\iota = 0$. To seek for the celestial position of GW source which leads to maximum resonance, we set $\iota = 0$, vary (ϑ, ϕ) and calculate $\Delta P_{\text{fin}}/P_0$ numerically. The result is visualized in Fig. 4, where the normal vector of $\mathbf{L2}$ is marked as a red star. As is expected, maximum resonance occurs when the binary and GW source are face-on.

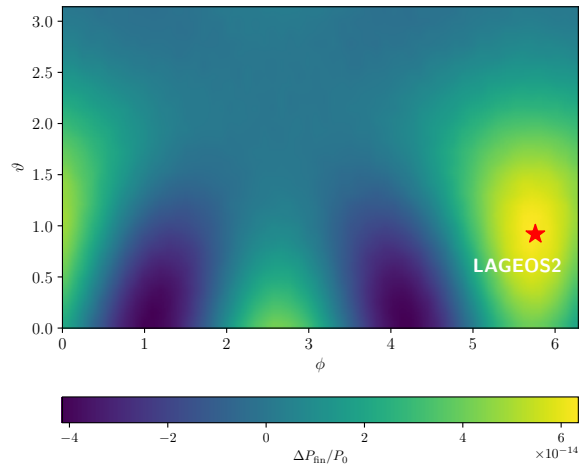


FIG. 4. The dependence of $\Delta P_{\text{fin}}/P_0$ on (ϑ, ϕ) . The normal vector of $\mathbf{L2}$ $((\vartheta, \phi) = (0.919, 5.760))$ is marked as a red star.

2. the argument of pericenter ω of test binary and the reference phase φ_{ref} of GW source

Eq.(7) indicates that the effects of ω and φ_{GW} on ΔP are degenerate, and the response of test binary depends on the combination $\varphi_{\text{GW}} - 2\omega$. This relationship also holds for chirping signals, only that $\varphi_{\text{GW}} - 2\omega$ should be replaced by or $2(\varphi_{\text{ref}} - \omega)$, since φ_{ref} is defined as the source’s orbital phase at reference frequency. To prove this, we vary $(\omega, \varphi_{\text{ref}})$ and keep their difference invariant. Shown in the upper panel of Fig. 5 are the results of 3 combinations: set 1: $(\pi/4, 0)$; set 2: $(0, -\pi/4)$; set 3: $(\pi/8, -\pi/8)$, and other parameters are the same as Tab. I. Obviously, the results of these combinations are indistinguishable.

Furthermore, we investigate the dependence of $\Delta P_{\text{fin}}/P_0$ on $2(\varphi_{\text{ref}} - \omega)$, which is equivalent to vary φ_{ref} and keep $\omega = 0$. It can be seen from the lower panel of Fig. 5 that $\Delta P_{\text{fin}}/P_0$ acts like a sinusoidal function of $2\varphi_{\text{ref}}$. In the rest of this paper, we will denote the values of $\{\vartheta, \phi, \iota, \omega, \varphi_{\text{ref}}\}$ which maximize $\Delta P_{\text{fin}}/P_0$ as the Optimal Parameters (**OP** hereafter).

3. the semi-major axis a of test binary

We consider four values of the semi-major axis: $a = \{0.782, 1.21, 2, 3, 4\} \times 10^4$ km. The 1st and 2nd of them correspond to the configurations of $\mathbf{L2}$ and **LARES** [43, 66], while the other three are assumed. Besides, for the convenience of further analysis, we set $\{\vartheta, \phi, \iota, \omega, \varphi_{\text{ref}}\}$ to **OP**, and other parameters are taken from Tab. I. Given the total mass of binary (which is approximately the mass of Earth), the orbital frequency, and hence the resonance frequency, is totally determined by a . Consequently, for different values of a , resonance mainly takes place at different stages of GW:

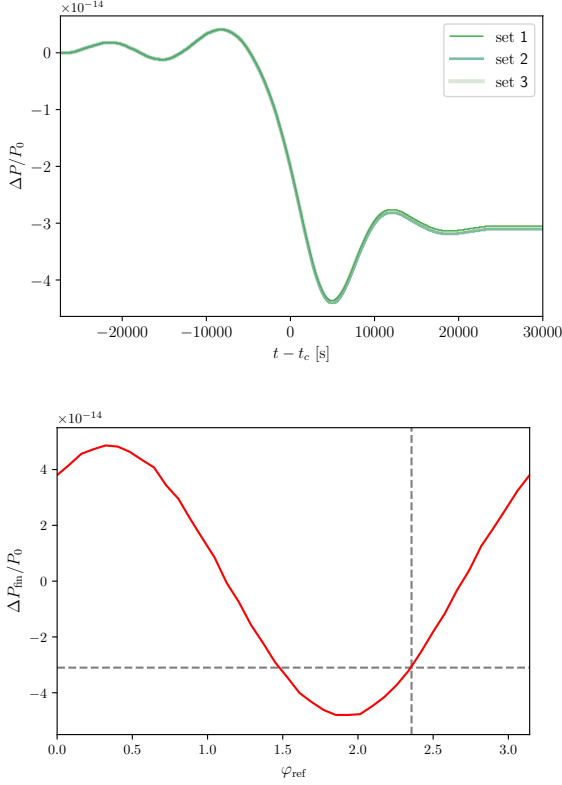


FIG. 5. Upper panel: $\Delta P/P_0$ under 3 sets of $(\omega, \varphi_{\text{ref}})$: set 1: $(\pi/4, 0)$; set 2: $(0, -\pi/4)$; set 3: $(\pi/8, -\pi/8)$. Lower panel: the dependence of $\Delta P_{\text{fin}}/P_0$ on φ_{ref} with $\omega = 0$. Set 2 of the upper panel is marked out with dashed lines.

1. Inspiral (e.g. $a = 4 \times 10^4$ km): f_{GW} increases slowly, thus resonance can last for a relatively long time ($\sim 10^5$ s), and $\Delta P_{\text{fin}}/P_0$ is the largest among all the a values in consideration;
2. Merger (e.g. $a = 1.21 \times 10^4$ km, 2×10^4 km, 3×10^4 km): The duration of resonance is shorter than case 1, while h_{GW} and \dot{h}_{GW} of this stage get much larger, thus the effect of resonance is only slightly weaker than case 1;
3. Near coalescence (e.g. $a = 0.782 \times 10^4$ km): In this extreme situation, resonance can only last for a very short duration, leading to a much smaller value of $\Delta P_{\text{fin}}/P_0$.

The above situations are illustrated in Fig. 6. For most of the cases, the values of $\Delta P_{\text{fin}}/P_0$ are at the same order, however, the absolute changes in a are considerably discrepant, i.e. when $a = \{0.782, 1.21, 2, 3, 4\} \times 10^4$ km, $\Delta a_{\text{fin}} = \{0.262, 5.023, 7.410, 13.11, 20.81\} \times 10^{-7}$ m.

4. BH masses M_{bh} and redshift z

For simplicity, we only consider equal-mass SMBHBs with component mass M_{bh} . Still, to explore the up-

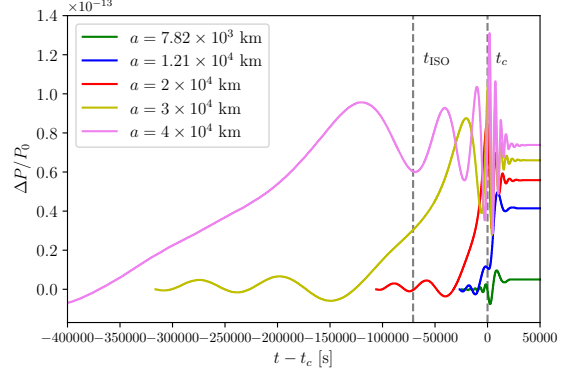


FIG. 6. The relative variations of P for $a = \{0.782, 1.21, 2, 3, 4\} \times 10^4$ km. The time of innermost stable circular orbit t_{ISO} and coalescence t_c are shown with dashed lines to roughly divide the incident GW into different stages.

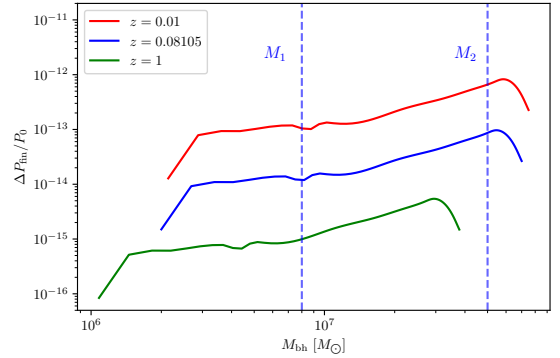


FIG. 7. The relationship between $\Delta P_{\text{fin}}/P_0$ and M_{bh} at redshifts 0.01, 0.08105 and 1.

per bound of response, the numerical calculations are based on **OP** and Tab. I. For sources at cosmological distances, M_{bh} enters the expression of GW in the form of redshifted mass $M_{\text{bh},z} \equiv (1+z)M_{\text{bh}}$. Theoretically, the influence of $M_{\text{bh},z}$ is twofold. Firstly, for different $M_{\text{bh},z}$, f_{res} appears at different stages of GW; secondly, the amplitude of GW is directly related to $M_{\text{bh},z}$. In addition, the amplitude is also inversely proportional to $d_L(z)$, which, at low redshifts, follows the Hubble law $d_L \propto z$. The relationship between $\Delta P_{\text{fin}}/P_0$ and M_{bh} at redshifts $z = 0.01, 0.08105, 1$ is shown in Fig. 7. At the redshift of **TS** ($z = 0.08105$), the range (M_1, M_2) marked in Fig. 7 represents the BH mass range where resonance starts at the merger stage, and a peak can be seen at around $M_{\text{bh}} = 5.7 \times 10^7 M_{\odot}$.

Appendix C: Signal-to-noise ratio of optimal matched filtering

The optimal SNR of matched filtering reads

$$\rho^2 = 4 \int_0^\infty \frac{|\delta\tilde{r}(f)|^2 df}{S_n(f)}. \quad (\text{C1})$$

where $\delta\tilde{r}(f)$ is the Fourier transform of residual distance $\delta r(t)$. $S_n(f)$ represents the one-sided noise power spectral density (PSD) of SLR, which is defined as twice the Fourier transform of autocorrelation function $R(\tau) = \langle n(t)n(t+\tau) \rangle$, $n(t)$ being the noise at time t . Following [26], the range measurements are assumed to be unbiased, with uncorrelated Gaussian noise of variance σ^2 . Thus, for discrete SLR data, by denoting the time interval between two adjacent measurements as t_s , $R(\tau)$ can be modeled as

$$R(\tau) = \begin{cases} \sigma^2, & |\tau| < t_s/2 \\ 0, & |\tau| \geq t_s/2 \end{cases}, \quad (\text{C2})$$

thus

$$S_n(f) = 2\sigma^2 t_s \text{sinc}(\pi t_s f). \quad (\text{C3})$$

Considering that the maximum frequency f_{\max} of $\delta\tilde{r}(f)$ is usually much smaller than $1/t_s$, we can approximate

$\text{sinc}(\pi t_s f)$ to 1, and it follows that

$$\begin{aligned} \rho^2 &\approx \frac{2}{\sigma^2 t_s} \int_0^{f_{\max}} |\delta\tilde{r}(f)|^2 df \\ &\approx \frac{1}{\sigma^2 t_s} \int_0^{T_{\text{obs}}} \delta r^2(t) dt \approx \frac{1}{\sigma^2} \sum_{i=1}^{N_{\text{obs}}} \delta r_i^2. \end{aligned} \quad (\text{C4})$$

where $\delta r_i \equiv \delta r(t_i)$, N_{obs} is the total number of normal point measurements, and $T_{\text{obs}} = t_s N_{\text{obs}}$. Note that to derive the second line, we have used the Parseval's theorem.

For the case shown in Fig. 2, when the scale of T_{obs} is much smaller than $P^2/\Delta P_{\text{fin}}$, the amplitude of δr increases linearly in time:

$$\delta r(t) = k T_{\text{obs}} \sin \frac{2\pi}{P_0} T_{\text{obs}}, \quad (\text{C5})$$

where k is the growth rate. Ignoring the oscillating terms, the quadratic sum of residuals reads

$$\sum \delta r_i^2 = \frac{k^2 t_s^2}{12} N_{\text{obs}} (N_{\text{obs}} + 1) (2N_{\text{obs}} + 1) \approx \frac{k^2 t_s^2}{6} N_{\text{obs}}^3. \quad (\text{C6})$$

As a result, the relationship between SNR and T_{obs} can be approximated as a power-law function:

$$\rho(T_{\text{obs}}) \approx \frac{k}{\sqrt{6} t_s \sigma} T_{\text{obs}}^{3/2} \propto T_{\text{obs}}^{3/2}. \quad (\text{C7})$$